Absolute/convective secondary instabilities and the role of confinement in free shear layers

Citation: Arratia, Cristóbal et al. "Absolute/convective secondary instabilities and the role of confinement in free shear layers." Physical Review Fluids 3, 5 (May 2018): 053901 © 2018 American Physical Society

As Published: http://dx.doi.org/10.1103/PhysRevFluids.3.053901

Publisher: American Physical Society

Persistent URL: http://hdl.handle.net/1721.1/115324

Version: Final published version: final published article, as it appeared in a journal, conference proceedings, or other formally published context

PHYSICAL REVIEW FLUIDS **3**, 053901 (2018)

Absolute/convective secondary instabilities and the role of confinement in free shear layers

Cristóbal Arratia,[1,2,*] Saviz Mowlavi,[2,3] and François Gallaire[2]
[1]*Nordita, KTH Royal Institute of Technology and Stockholm University, Roslagstullsbacken 23, SE-106 91 Stockholm, Sweden*
[2]*Laboratory of Fluid Mechanics and Instabilities, EPFL, 1015 Lausanne, Switzerland*
[3]*Department of Mechanical Engineering, Massachusetts Institute of Technology, Cambridge, Massachusetts 02139, USA*

(Received 19 July 2017; published 7 May 2018)

We study the linear spatiotemporal stability of an infinite row of equal point vortices under symmetric confinement between parallel walls. These rows of vortices serve to model the secondary instability leading to the merging of consecutive (Kelvin-Helmholtz) vortices in free shear layers, allowing us to study how confinement limits the growth of shear layers through vortex pairings. Using a geometric construction akin to a Legendre transform on the dispersion relation, we compute the growth rate of the instability in different reference frames as a function of the frame velocity with respect to the vortices. This approach is verified and complemented with numerical computations of the linear impulse response, fully characterizing the absolute/convective nature of the instability. Similar to results by Healey on the primary instability of parallel tanh profiles [J. Fluid Mech. **623**, 241 (2009)], we observe a range of confinement in which absolute instability is promoted. For a parallel shear layer with prescribed confinement and mixing length, the threshold for absolute/convective instability of the secondary pairing instability depends on the separation distance between consecutive vortices, which is physically determined by the wavelength selected by the previous (primary or pairing) instability. In the presence of counterflow and moderate to weak confinement, small (large) wavelength of the vortex row leads to absolute (convective) instability. While absolute secondary instabilities in spatially developing flows have been previously related to an abrupt transition to a complex behavior, this secondary pairing instability regenerates the flow with an increased wavelength, eventually leading to a convectively unstable row of vortices. We argue that since the primary instability remains active for large wavelengths, a spatially developing shear layer can directly saturate on the wavelength of such a convectively unstable row, by-passing the smaller wavelengths of absolute secondary instability. This provides a wavelength selection mechanism, according to which the distance between consecutive vortices should be sufficiently large in comparison with the channel width in order for the row of vortices to persist. We argue that the proposed wavelength selection criteria can serve as a guideline for experimentally obtaining plane shear layers with counterflow, which has remained an experimental challenge.

DOI: 10.1103/PhysRevFluids.3.053901

---

[*] cristobal.arratia@gmail.com

2469-990X/2018/3(5)/053901(24)

I. INTRODUCTION

Free shear or mixing layers form when two volumes of fluid traveling parallel to each other at different speeds are put in contact. They appear in a large variety of natural and technological contexts. In addition, they constitute a basic building block for understanding other flows such as wakes, jets, or separation regions, since they provide the most basic example of shear flow instability: the instability of an inflection point in the velocity profile violating Rayleigh's criterion for stability of inviscid plane flow [1]. Known as Kelvin-Helmholtz (KH) instability, it leads to the roll-up of the vorticity of the shear layer into a row of consecutive vortices of the same sign [2,3], the KH vortices, often referred to as billows or rollers.

A large body of work has been dedicated to the instabilities of mixing layers, which can be broadly divided into studies concerned with (i) the primary instability of the parallel or weakly nonparallel flow fields [4–7] and (ii) secondary instabilities of the already formed KH vortices [8–11], which form later in time or further downstream. The term "secondary instabilities" refers, in general, to instabilities of a certain flow (or state) that is itself the result of another instability, the "primary instability" of a simpler base flow. Therefore, the existence and properties of any secondary instability are greatly determined by the specific development of the primary instability. In the present case of free shear layers, several analyses of primary (i) and secondary (ii) instabilities have also included the effects of varying fluid properties like density or viscosity, but we will only consider the case of homogeneous shear layers in which the two flow streams are composed of the same fluid.

A. Spatiotemporal instabilities

In this context, the main aspect of the primary instability (i) that has remained a subject of research during the past few decades is its spatiotemporal properties [5–7]. This sprung from the seminal recognition by Huerre and Monkewitz [5] of the importance of the distinction between absolute and convective instabilities [12], previously developed in plasma physics [13]. This distinction arises in the theory of spatiotemporal instabilities, which provides a synthesis of temporal and spatial stability analyses previously in use for spatially extended shear flows. Temporal stability analyses, which consider a real wave number k and a complex frequency ω in the dispersion relation, are more suitable for problems of initial value type, while open flows with an inlet condition or a harmonic forcing are better treated with a spatial analysis considering real ω and complex k [14]. Accordingly, temporal analyses predict growth rates in time for perturbations which are periodic in space, while spatial analyses provide growth rates in space for harmonic fluctuations with an amplitude that is constant in time. In the more general spatiotemporal stability analyses, the dispersion relation is considered with both ω and k complex. The growth rate on any particular reference frame can be determined from the dispersion relation $\omega(k)$ evaluated at the *absolute wave number* k_0, which satisfies the key property of zero group velocity $\frac{d\omega}{dk}|_{k_0} = 0$ in that reference frame. A temporal instability (i.e., real k with positive growth rate) will then be absolute (respectively, convective) if the *absolute growth rate* given by the imaginary part of $\omega(k_0)$ is positive (resp., negative) in the selected reference frame, usually the one singled out by boundary conditions or forcing. We note that, for spatially developing flows, these linear analyses rely on a *local* approximation in which the flow is assumed parallel and infinite at each streamwise station; this approximation can serve as the zeroth order of a *global* approximation including nonparallel effects and comprising the full domain. In this context, a region of local absolute instability can explain the appearance of a linearly unstable global mode [12].

An important insight in spatiotemporal stability analyses is that local spatial stability (real ω and complex k) is directly applicable only when the instability is convective [5], since the linearized response to a constant disturbance diverges in time at positions where the instability is absolute [14]. The consequences can be dramatic for spatial flows, i.e., flows consistent with a long time limit. When absolutely unstable, these flows generally display self-excited oscillations that are fairly insensitive to weak or relatively moderate extrinsic disturbances. This self-sustained intrinsic behavior cannot be captured within a purely local and linear approach. Consideration of nonparallel and nonlinear effects is required; in the weakly nonlinear realm, this behavior can be understood as the nonlinear saturation of a linearly unstable spatially extended mode, while in the weakly nonparallel framework, it can be interpreted as a nonlinear front between linear instability waves and fully nonlinear wave solutions [15]. Convectively unstable flows, on the contrary, are highly sensitive to external disturbances (forcing or noise) which are constantly and selectively amplified while advected through the domain. This was early recognized in simulations of the complex Ginzburg-Landau model by Deissler [16], who coined term "noise-sustained structures." Since convectively unstable flows generally possess a range of amplified frequencies, they behave like a bandpass amplifier displaying a broad spectrum of disturbances [12,14]. In the case of free shear layers, the absolute/convective instability calculation by Huerre and Monkewitz [5] gave an excellent prediction of the experimentally observed transition threshold from a bandpass noise amplifier to a self-sustained peaked oscillator as the counterflow is increased [17], that is, as the mean velocity of the two streams is reduced while maintaining the same amount of shear.

The transition observed in Ref. [17] gave the first direct experimental confirmation of the fundamental role of the absolute/convective nature in the spectral signature of instabilities in open flows. More recently, Healey [6] demonstrated that a moderate amount of confinement in the shearing direction promotes the absolute nature of the instability, without however providing any experimental evidence. But as remarked previously by Juniper [18,19], a similar destabilizing effect of confinement is present in jets and wakes, for which there are indeed experimental indications of such an effect (see Ref. [18], and references therein). Unsurprisingly, these flows are all stabilized for sufficiently strong confinement.

B. Vortex pairing instability in free-shear layers

In free shear layers, studies of secondary instabilities (ii) have uncovered several physical mechanisms, such as for instance the elliptic and hyperbolic instabilities, which break the translational invariance in the spanwise direction through three-dimensional (3D) instabilities [9–11]. A seminal contribution here is the study of Pierrehumbert and Widnall [9] focused on the 3D stability of Stuart vortices [20]. These vortices are given by a one-parameter family of two-dimensional (2D) solutions to the Euler equations proposed to represent a periodic array of 2D vortices separating two counterflows, with a parameter $\rho \in [0,1]$ measuring the dimensionless vortex core size. The solution for $\rho = 1$ consists of a periodic row of infinitely concentrated point vortices, while $\rho = 0$ corresponds to the hyperbolic-tangent parallel velocity profile. While 3D instabilities are determinant in the route to turbulence that leads to disorder and mixing at small scales [10], at large scales (larger than the KH billows) the flow remains 2D and to a great extent organized, even in highly turbulent cases [2,21]. We focus our attention here on these large scales, in particular, on the 2D pairing instability associated with the growth of the first subharmonic [22]. Eventually, this instability, which is a particular type of secondary instability, saturates and leads to the merger of primary vortices into larger vortices with twice the initial spacing [8].

Since it leads to a similar row of vortices as that from which it develops, this secondary instability can then repeat itself in a sequence of successive instabilities. These subsequent instabilities could be thought of as "tertiary," "quaternary," and so on, but we will refer to them simply as the secondary vortex pairing instability or 2VPI for short. The successive occurrences of the 2VPI can develop in time or in space depending on whether the experimental setting is temporal or spatial. The first case is the temporal shear layer, as in numerical simulations [23] and tilt-tank experiments [24], in which there is usually no mean advection and each (numerical or physical) experiment is a one-time transient. The second case, that of spatial mixing layers, is the most thoroughly studied experimentally [3], most often as coflowing mixing layers. These experiments can in principle last for an arbitrarily large amount of time, during which subsequent instabilities succeed one after another in different and more or less stationary regions of space. In this context, the pairing instability was described by Winant and Browand [8] as the key mechanism of spatial growth for turbulent mixing layers, receiving subsequently a great deal of attention [3,21]. In the absence of forcing, Winant and

Browand report a large variability on the pairing locations and observed up to four pairings [8]. In experiments on an axisymmetric air jet at $\mathrm{Re} = 50\,000$ with an applied periodic forcing, Kibens [25] identified a sequence of three successive vortex-pairing events at well fixed downstream locations. These examples [8,25] show precisely the large variability and high receptivity to forcing that are now well understood as the footprint of the bandpass noise-amplifier behavior of convective instabilities described above. It is interesting to note that the previously mentioned [17] experimental confirmation of a transition from a bandpass noise amplifier to a self-sustained peaked oscillator with increasing counterflow was achieved on a spatial axisymmetric air jet. An earlier attempt at generating a spatial mixing layer with counterflow failed, resulting instead in a flow with a totally different configuration consisting roughly in a single stagnation point with hyperbolic streamlines [26]. A planar mixing layer with counterflow was achieved much later with a more elaborate confining geometry [27].

C. Absolute/convective secondary instabilities

As stated above, the distinction between absolute and convective instabilities has been found determinant in the behavior of many unstable open flows [12,15], but the vast majority of studies have focused on its effect on primary instabilities. The absolute/convective nature of secondary instabilities have in general received far less attention, although they can grow not only in time but also in space, just as primary instabilities. In the words of Huerre [28], “primary and secondary instabilities arising in fluid flows need not have the same absolute/convective character.” Some absolute/convective analyses of secondary instabilities include those of the Ekhaus and zigzag instabilities [29], the subharmonic instability of a periodic array of vortex rings [30], or the von Karman street of alternating point vortices [31]. There are no major difficulties when the secondary instability is convective. Indeed, causality implies that a temporal sequence of instabilities can translate into a spatial one if the instabilities are convective [32]. In this case, the secondary instability may develop downstream on the saturated state without affecting its precursor, the primary instability upstream. We have previously shown [31] that this is the case for the Kármán street of point vortices [33] modeling vortex shedding phenomena: The well-known (secondary) instability [22] was shown to be strongly convective when applied to wakes [31], thus reconciling the intrinsic instability of Kármán’s point-vortex model with ubiquitous observations of vortex shedding behind obstacles. It has been recently confirmed experimentally [34] that this instability can be also stabilized by strong confinement, even in the absence of mean advection.

The situation is considerably more complex if the secondary instability is absolute. From a certain perspective this can be seen as somewhat paradoxical, since an instability propagating upstream would disrupt its (primary) precursor [32]. This situation has been studied by Chomaz and coworkers [29,32,35], who have proposed that it constitutes a possible scenario for abrupt transition [15,36]. According to Chomaz *et al.*’s description, if the secondary instability is already absolute when the primary instability transitions from convective to absolute, perturbations in the lee of the primary front never fade away and are likely to yield a complex, disordered behavior. An example of this was observed by Couairon and Chomaz in a complex Ginzburg-Landau model [35], in which the system presented aperiodic behavior when the primary nonlinear wave was subject to absolute secondary instability. Moreover, in the words of his review [15], p. 385, this “one-step scenario to disorder, involving a global mode made of a wave already absolutely unstable to secondary instability at the global threshold, may also explain the abrupt transition to turbulence observed in the rotating disk.” Chomaz then refers to theoretical and experimental studies by Lingwood, showing that turbulence in rotating disk flow occurs close to where the flow becomes absolutely unstable [37,38], and work by Pier, showing that there is an absolute secondary instability in this flow and proposing it as the mechanism of direct transition [39]. Recent investigations [40–42] yield support to this scenario, although the secondary instability is not the subharmonic one predicted by Pier [39] and its nature is not yet clear. In any case, the outcome of an absolute secondary instability cannot be predicted *a priori*; it should be studied on a case-by-case basis with consideration of global and nonlinear effects.

D. The present work

Returning to free shear layers, Brancher and Chomaz [32] have indeed shown that the 2VPI is more prompt to become absolute than the primary instability. More precisely, they have determined the absolute/convective nature of the subharmonic pairing instability of a row of finite-size corotating vortices, viewed as the saturation of the primary Kelvin-Helmhotz instability. For that purpose, they used the family of Stuart vortices and performed a spatiotemporal stability analysis through the numerical calculation of the linearized impulse response, thereby generalizing the temporal stability analysis of Ref. [9]. They found that the backflow needed to trigger absolute instability was monotonically decreasing when the vortex concentration was increasing. In particular, the secondary pairing instability was found already absolutely unstable for backflows for which the primary instability was still convective. According to Chomaz [15], p. 384, “these results on the pairing instability explain why the 2D Global mode in the parallel mixing layer computed [in Ref. 36] is irregular at threshold, with pairings occurring randomly.” We will come back to this quotation and argue that a different interpretation is also possible in this case. In particular, the effects of confinement have not been explored, and as the spacing between consecutive vortices increases, these should eventually become important. *The near self-similarity of the sequential process of mixing layer growth through vortex pairings is most naturally broken by the external length-scale imposed by confinement*. As we shall see, consideration of confinement provides a mechanism for wavelength selection in spatially developing shear layers with counterflow.

In the present work, we study the effect of confinement on the absolute/convective nature of the 2VPI. To that end, we model the row of KH vortices resulting from the primary instability with a periodic row of point vortices, which in the absence of confinement has a single length scale and is therefore self-similar. In Sec. II, we describe our model and formulate the linear stability problem, yielding the relevant dispersion relation. Since the subharmonic instability of the confined row of point vortices can be (and is) studied independently of the primary instability in shear layers, we refer to it as the subharmonic pairing instability, or SPI, and leave the acronym 2VPI for making explicit reference to the secondary instability relevant to free shear layers. We compute the growth rate of the SPI in different reference frames in Sec. III. For this, we develop in Sec. III A a geometrical method consisting essentially of a Legendre transformation that effectively switches the dependence on the imaginary part of the complex wave number by a dependence on the propagation velocity of a moving frame. A more challenging application of this method is given for the Kármán street of point vortices in Appendix A. In Sec. IV, we compare the spatiotemporal properties of the SPI with corresponding results for a parallel tanh profile [6] and discuss the possible implications of our results, including a wavelength selection mechanism that provides a criteria for the admissibility of plane shear layers (in the form of vortex rows) with counterflow. We summarize and conclude in Sec. V.

II. PROBLEM FORMULATION

A. Governing equations

We consider the system shown in Fig. 1, composed of an infinite row of point vortices of circulation Γ symmetrically enclosed between two horizontal confining walls. The distance between consecutive vortices is a and that between the two walls is d. The confinement is imposed by assigning to each vortex an infinite series of image vortices above and below the walls. This gives rise to a doubly infinite array of vortices situated at coordinates (ma,nd) and of strength $(-1)^n\Gamma$, where $m,n \in \mathbb{Z}$ and $n = 0$ corresponds to the physical vortices.

This array of vortices corresponds to a static equilibrium configuration since the velocity induced on any of the physical vortices by all other vortices is zero. When we apply a perturbation (x_m, y_m) to the positions of the physical vortices, the coordinates of the vortices become $(ma + x_m, nd + (-1)^n y_m)$, wherein all the image vortices are duly tied to their corresponding physical vortex. Without

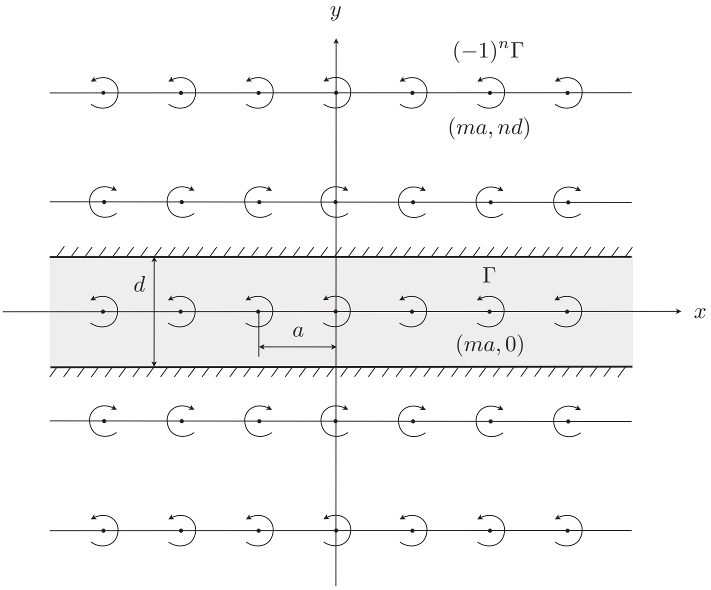

FIG. 1. Confined single row of point vortices.

loss of generality, the equations of motion of the $m = 0$ physical vortex are

$$\frac{dx_0}{dt} = -a^2\omega_0 \sum_{m=-\infty}^{\infty} \sum_{n=-\infty}^{\infty}{}'' (-1)^n \frac{y_0 - nd - (-1)^n y_m}{r_{m,n}^2}, \tag{1a}$$

$$\frac{dy_0}{dt} = a^2\omega_0 \sum_{m=-\infty}^{\infty} \sum_{n=-\infty}^{\infty}{}'' (-1)^n \frac{x_0 - ma - x_m}{r_{m,n}^2}, \tag{1b}$$

where

$$r_{m,n}^2 = [nd + (-1)^n y_m - y_0]^2 + (ma + x_m - x_0)^2 \tag{2}$$

is the squared distance between the $m = 0$ physical vortex and the (m,n) vortex, and $\omega_0 = \Gamma/(2\pi a^2)$. The double prime on the summation sign means that $n = 0$ is excluded when $m = 0$. In the following, all quantities are nondimensionalized with the length a and the characteristic time $1/\omega_0$. The system is entirely specified by a single parameter, the confinement ratio $q = d/a$.

Assuming infinitesimal perturbations, Eqs. (1) can be linearized about the equilibrium configuration to yield

$$\frac{dx_0}{dt} = -\frac{\pi^2}{2q^2} y_0 - \sum_{m=-\infty}^{\infty}{}' \sum_{n=-\infty}^{\infty} \frac{n^2q^2 - m^2}{(n^2q^2 + m^2)^2} [y_m - (-1)^n y_0], \tag{3a}$$

$$\frac{dy_0}{dt} = \sum_{m=-\infty}^{\infty}{}' \sum_{n=-\infty}^{\infty} (-1)^n \frac{-n^2q^2 + m^2}{(n^2q^2 + m^2)^2} (x_m - x_0), \tag{3b}$$

where the prime on the summation sign means $m = 0$ is excluded. The series of images of the $m = 0$ vortex yields the first term in Eq. (3a). Summing the series over n in the software MATHEMATICA gives

$$\frac{dx_0}{dt} = \frac{\pi^2}{q^2}\sum_{m=-\infty}^{\infty}{}' C_m y_m - \frac{\pi^2}{q^2}\left[\frac{1}{2} + \sum_{m=-\infty}^{\infty}{}' D_m\right] y_0, \tag{4a}$$

$$\frac{dy_0}{dt} = \frac{\pi^2}{q^2}\sum_{m=-\infty}^{\infty}{}' D_m(x_m - x_0), \tag{4b}$$

where

$$C_m = \operatorname{csch}^2\left(\frac{m\pi}{q}\right) \tag{5a}$$

and

$$D_m = \frac{1}{4}\left[\operatorname{csch}^2\left(\frac{m\pi}{2q}\right) + \operatorname{sech}^2\left(\frac{m\pi}{2q}\right)\right]. \tag{5b}$$

These equations, defined here for the $m = 0$ vortex, apply to each vortex m and define the infinite set of linear equations governing the evolution of infinitesimal perturbations to the confined single row of point vortices.

B. Dispersion relation and temporal stability

Let us now look for solutions to the perturbation Eqs. (4) of the form

$$\begin{bmatrix} x_m \\ y_m \end{bmatrix} = \begin{bmatrix} \alpha \\ \beta \end{bmatrix} e^{i(km-\omega t)}, \tag{6}$$

where k and ω are the wave number and frequency, respectively. When we introduce (6) into (4), the governing equations are reduced to two coupled equations for α and β

$$\begin{bmatrix} i\omega & A \\ B & i\omega \end{bmatrix}\begin{bmatrix} \alpha \\ \beta \end{bmatrix} = \begin{bmatrix} 0 \\ 0 \end{bmatrix}, \tag{7}$$

where the coefficients A and B are given by

$$A = \frac{\pi^2}{q^2}\left[\sum_{m=-\infty}^{\infty}{}' C_m e^{ikm} - \frac{1}{2} - \sum_{m=-\infty}^{\infty}{}' D_m\right], \tag{8a}$$

$$B = \frac{\pi^2}{q^2}\sum_{m=-\infty}^{\infty}{}' D_m(e^{ikm} - 1), \tag{8b}$$

with C_m and D_m defined in Eqs. (5). The existence of nontrivial solutions to Eq. (7) requires the determinant of the matrix to be zero, imposing the dispersion relation

$$\omega = \pm i\sqrt{AB}. \tag{9}$$

The temporal stability of the confined single row of vortices is determined by assigning a real value to the perturbation wave number k and evaluating the growth rate of the perturbation, given by the imaginary part of ω. We restrict ourselves to values of k between 0 and π since disturbances of wave number $2\pi - k$ are equivalent to the complex conjugate of disturbances of wave number k.

In Fig. 2(a), we plot the growth rate ω_i versus the wave number k, for different values of the confinement ratio q. In all cases, the growth rate has a maximum at $k = \pi$ which corresponds to the SPI [8,22]. While the growth rate decreases with the confinement ratio q, the instability is not totally suppressed. Indeed, the product AB is always a positive real number. Thus, the two solutions

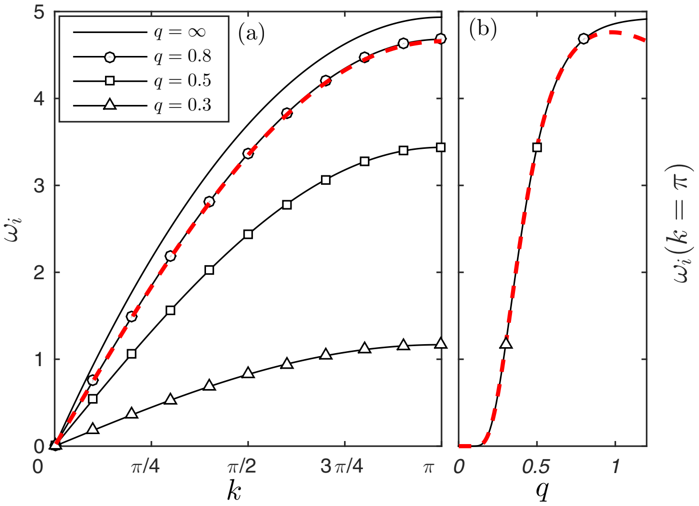

FIG. 2. Temporal dispersion relation. (a) Growth rate ω_i vs wave number k for different confinement ratios. (b) Its value at $k = \pi$ vs confinement ratio q.

for ω are purely imaginary complex conjugates and the confined single row of vortices is temporally unstable for all finite values of q. This implies that the SPI is present regardless of how far apart along the channel are consecutive vortices, which is somewhat surprising, However, a simple analysis of the dispersion relation shows that the growth rate of the instability quickly goes to zero as $q \to 0$. For small q, each of the series coefficients C_m and D_m [defined in Eqs. (5)] goes to zero exponentially and the series is dominated by the very first terms. Truncating the series while leaving the first two dominant terms with k dependence gives the dispersion relation as

$$\omega_i \sim \pm\frac{\pi^2}{q^2}\exp\left(-\frac{\pi}{2q}\right)\sqrt{2(1-\cos k)(1+8e^{-\pi/q})+4\sin^2(k)\,e^{-\pi/q}}, \tag{10}$$

when $q \to 0$, showing that the growth rate ω_i is exponentially small for strong confinement. As shown in the dashed lines of Fig. 2(a), Eq. (10) matches very well the temporal dispersion relation for a confinement ratio as large as $q = 0.8$, which is already quite close to the dispersion relation of the unconfined case $q = \infty$.

The unconfined limit is attained remarkably fast, as can be seen from the maximum growth rate $\omega_i(k = \pi)$ as a function of q shown in Fig. 2(b). The maximum ω_i for $q = 1.2$, at the end of the plotted range in Fig. 2(b), is almost the same as the $\omega_i(k = \pi)$ of the unconfined limit $q = \infty$ shown in Fig. 2(a). In the unconfined limit, the hyperbolic-cosecant terms [Eqs. (5)] diverge as q^2/m^2 when $q \to \infty$. Keeping these leading terms compensates the q^2 in the denominator of A and B [Eqs. (8)] and one recovers the unconfined dispersion relation given by Saffman [22]

$$\omega_i = \pm\frac{k}{2}(2\pi - k), \tag{11}$$

valid in the limit $q = \infty$. Keeping extra terms gives either vanishing or divergent contributions. Thus, we have not been able to obtain a correction of this dispersion relation in the case of weak confinement. This is probably related to how quickly the confined dispersion relation approaches that of the unconfined case.

III. SPATIOTEMPORAL STABILITY

In practice, the absolute or convective (A/C) nature of an instability is determined in two different ways: finding the *absolute growth rate* from the complex dispersion relation [12] and from a numerically computed impulse response [32,43]. Whereas the computation from the numerical impulse response involve simulations in sufficiently large domains and for sufficiently large times, it readily provides the perturbation growth rate in different reference frames. The determination of the A/C character of an instability in a given frame is generally more efficient from the dispersion relation, but computing the growth rate in different reference frames usually involves the recomputation of the dispersion relation for each particular frame. This needs not to be the case, since the complex dispersion relation encodes the stability properties in all frames. Indeed, a change of reference frame in the dispersion relation corresponds to a simple Doppler shift. In the following, we present a simple but general geometric construction, akin to a Legendre transform, which allows us to retrieve the growth rate of an instability in different reference frames from the dispersion relation computed on a single frame.

A. Growth rate in different reference frames from the dispersion relation

In the laboratory reference frame (at rest), the absolute growth rate is given by

$$\sigma = \omega_i(k_0), \tag{12}$$

where k_0 is the absolute wave number that satisfies the zero group velocity condition

$$\frac{d\omega}{dk}(k_0) = 0 \tag{13}$$

and the pinch point criterion [13,14]. If we consider now a reference frame moving at a velocity v, the dispersion relation in the new frame is given by a Doppler shift

$$\omega^v(k) = \omega(k) - vk, \tag{14}$$

where ω is the the dispersion relation in the rest frame.

In the moving frame, the absolute wave number $k_0^v = k_{0r}^v + ik_{0i}^v$ satisfying the zero group velocity condition is now given by

$$\frac{d\omega^v}{dk}\left(k_0^v\right) = 0, \tag{15}$$

or equivalently from Eq. (14)

$$\frac{d\omega}{dk}\left(k_0^v\right) = v, \tag{16}$$

stating that the zero group velocity in the moving frame corresponds to a group velocity v in the laboratory frame [14]. The growth rate in the reference frame moving with velocity v is then given as in Eq. (12) by

$$\sigma(v) = \omega_i^v\left(k_0^v\right) = \omega_i\left(k_0^v\right) - vk_{0i}^v. \tag{17}$$

Thus, $\sigma(v)$ is usually obtained by calculating the Doppler-shifted dispersion relation ω^v separately for given values of v, then using (15) to obtain k_0^v, and finally the left equality in Eq. (17) to find the growth rates $\sigma(v)$ relating to these values of v.

We now present an alternative method for obtaining the growth rate σ directly *as a function* of v. Assuming that $\omega(k)$ is an analytic function of k, condition Eq. (16) can be written in terms of the imaginary part of ω and its derivatives as

$$\frac{\partial\omega_i}{\partial k_i}\left(k_0^v\right) = v, \tag{18a}$$

$$\frac{\partial\omega_i}{\partial k_r}\left(k_0^v\right) = 0. \tag{18b}$$

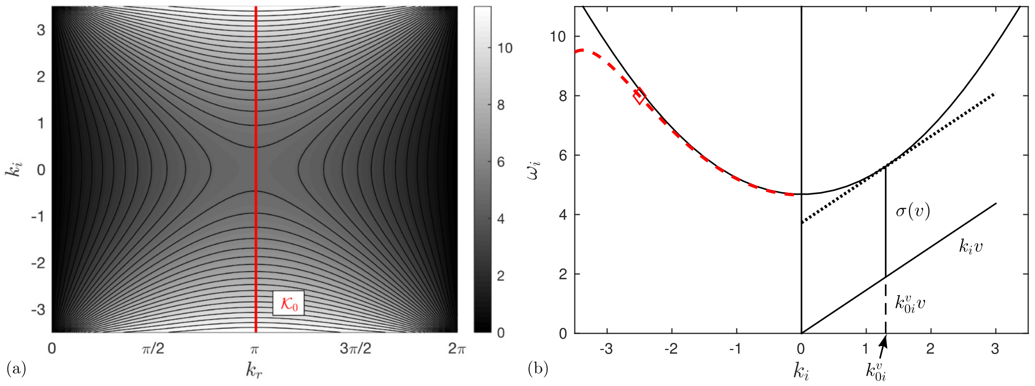

FIG. 3. (a) Isocontours of ω_i in the complex k plane, calculated from the dispersion relation (9) for $q = 0.8$. The solid red line represents the locus of absolute wave numbers defined by (19). (b) Geometrical construction to determine the growth rate $\sigma(v)$ from $\omega_i(k_{0r}^v(k_i),k_i)$. The k_{0i}^v pertaining to a particular v is given by (18a), and the corresponding growth rate is obtained from (17). The dashed line on the left side of the plot shows the ω_i given by approximation (10), with the diamond indicating the inflection point determining the validity limit of the approximation (see text).

Imposing condition (18b), which is independent of v, determines the locus of absolute wave numbers

$$\mathcal{K}_0 = \left\{ k_0^v = k_{0r}^v + i k_{0i}^v : \frac{d\omega}{dk}\left(k_0^v\right) = v \right\}, \tag{19}$$

which is a (one-dimensional) curve in the complex k plane that contains the union of absolute wave numbers in any moving frame.

The locus $\mathcal{K}_0$ of absolute wave numbers of the dispersion relation Eq. (9) is shown as the solid red line in Fig. 3(a), together with the contour levels of $\omega_i(k)$ for $q = 0.8$. Because of the symmetry of the perturbations around $k = \pi$, condition (18b) is satisfied for $k_r = \pi$ and $\mathcal{K}_0$ involves different values of k_i with k_r constant. It will be usually possible to parametrize $\mathcal{K}_0$ in terms of k_i, although it can also happen that $\mathcal{K}_0$ contains multiple values of k_r for some interval of k_i, as shown in the example of Appendix A. In either case, the imaginary part of the frequency can be expressed from the dispersion relation as a (possibly multivalued) function of k_i as $\omega_i(k_{0r}^v(k_i),k_i)$. Note that when restricted to $k^v \in \mathcal{K}_0$, it follows from Eq. (18b) that

$$d\omega_i = \frac{\partial \omega_i}{\partial k_i} dk_i, \tag{20}$$

so that the imaginary frequency ω_i varies through the variation of k_i only and not through k_{0r}^v. Thus, it is natural to view $\omega_i(k_{0r}^v,k_{0i}^v)$ as a one-variable function and k_i as the independent variable. We can now rewrite the growth rate in Eq. (17) as

$$\sigma(v) = \omega_i\left(k_{0r}^v(k_i),k_i\right) - v k_i, \tag{21}$$

where $v = \frac{\partial \omega_i}{\partial k_i}$. Equation (21) is in the form of a Legendre transform exchanging ω_i by the growth rate σ and k_i by its conjugate variable v. As shown in Fig. 3(b), it corresponds to a simple geometrical construction to determine k_{0i}^v and the growth rate σ for the corresponding v. The solid curve shows $\omega_i(k_r = \pi,k_i)$ from the dispersion relation (9) for $q = 0.8$, and the straight line represents $k_i v$ for a given v, i.e., the second term in Eq. (21). Condition (18a) corresponds to choosing k_{0i}^v as the k_i for which the ω_i curve is parallel to this line. The growth rate along the spatiotemporal ray $x/t = v$ is then given by Eq. (17) as the vertical distance between ω_i and the straight line, evaluated at k_{0i}^v.

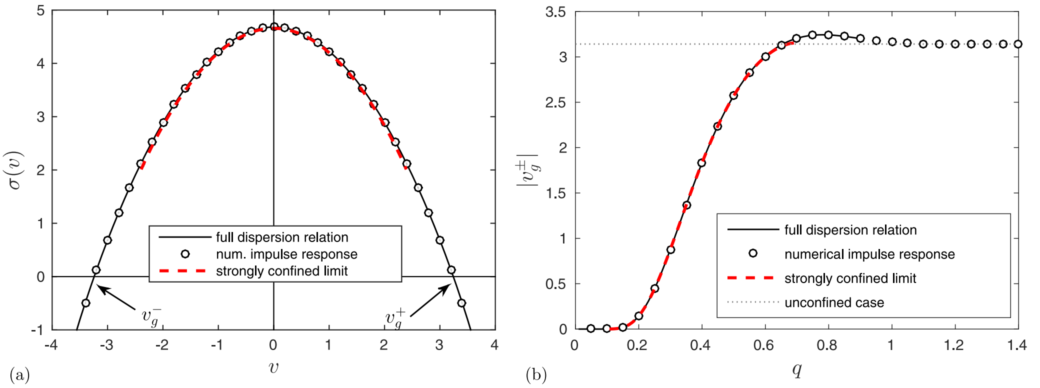

FIG. 4. (a) Growth rate $\sigma(v)$ of the impulse response wave packet along spatiotemporal rays $x/t = v$ for a confinement ratio $q = 0.8$. The streamwise extent of the wave packet is given by the leading- and trailing-edge velocities $v_g^{\pm}$ such that $\sigma(v_g^{\pm}) = 0$. Results from imposing the transformation (21) to the exact (solid line) and approximate (dashed line) dispersion relations and from numerical simulations of the impulse response (circles). (b) Magnitude of the leading- and trailing-edge velocities $|v_g^{\pm}|$ of the impulse response wave packet versus the confinement ratio q. Results from the analytical dispersion relation with the graphical method (solid line) are compared with those from numerical simulations of the impulse response (circles). As q increases, $|v_g^{\pm}|$ quickly approaches the theoretical value of π for the unconfined single row of point vortices [44].

The solid line in Fig. 4(a) shows $\sigma(v)$ resulting from the application of this technique to the dispersion relation (9) for the case $q = 0.8$. Because of the upstream-downstream symmetry of the system, ω_i and $\sigma(v)$ are even respectively in k_i and v. Also shown in Fig. 4(a), in the dashed line, is the corresponding growth rate obtained from the dispersion relation (10) asymptotically valid in the limit of strong confinement. The agreement for the plotted values is very good. However, the approximate curve of $\sigma(v)$ does not extend to larger values of $|v|$ because the corresponding $\omega_i(k_0^v(k_i))$ presents an inflection point corresponding to a maximum of $|\frac{\partial \omega_i}{\partial k_i}|$, shown with a diamond in the left side of Fig. 3(b). Beyond this point, the approximation given by Eq. (10) is meaningless.

For large times, the spatiotemporal region of growth of an initial impulse localized at $(x,t) = (0,0)$ is given by the spatiotemporal rays x/t of leading- and trailing-edge velocities $v_g^{\pm} = x/t$ such that $\sigma(v_g^{\pm}) = 0$. Note that applying this marginal stability condition $\sigma(v_g^{\pm}) = 0$ in Eq. (21), one recovers the Dee and Langer [45] and van Saarlos [46] condition $v_g = d\omega/dk = \omega_i/k_i$ for the linearly selected velocity of front propagation.

The magnitude of the leading- and trailing-edge velocities $|v_g^{\pm}|$ is reported in Fig. 4(b) for a range of confinement ratios. The solid and dashed lines show the values obtained from the full dispersion relation (9) and from its strong confinement approximation (10), respectively. In the strong confinement limit, this propagation velocity decreases rapidly when $q \lesssim 0.6$, a trend which is quantitatively well captured by the approximated dispersion relation (10) (dashed line). This approximation works well until $q = 0.69$, after which the approximation loses validity before the the marginal stability criterion is satisfied. For slightly larger confinement ratios, the full dispersion relation (9) (solid line) reveals that $|v_g^{\pm}|$ reaches a maximum of $|v_g^{\pm}| = 3.243$ around $q = 0.78$. Remarkably, this value is larger than that of the unconfined case [44], which is given by $|v_g^{\pm}| = \pi$ and represented by the horizontal dotted line in Fig. 4(b). This increase in the propagation velocity of the instability is a destabilizing effect of confinement analogous to that found for parallel flows, as we will discuss in detail below in Sec. IV A. Past this maximum in $|v_g^{\pm}|$, a small decrease can be observed before the evaluation fails because of the divergence of the series in the dispersion relation (9). Indeed, the terms of the series grow exponentially with m when $|k_i| > \pi/q$, rendering the evaluation impossible through a direct summation for values of q greater than 0.9. Therefore, in order to complete the curve, we turn in the next section to a different approach that relies on direct numerical simulations of the impulse response.

B. Growth rates from the numerically computed impulse response

The asymptotic properties of the impulse response wave packet can also be retrieved from a numerical simulation of the response of the system to a localized initial perturbation [32,43]. This method was recently implemented for the secondary instability of the confined Kármán street [31], using a point vortex model closely related to the system presently under study. Hence we adopt a similar approach and compute the time evolution of the single row of vortices through direct time integration of the linearized perturbation equations (4). We use a finite number of physical vortices and simulate the infinite series in the perturbation equations through additional virtual vortices that are slaved to the physical ones (for additional details, see Ref. [31]). The equations of motion (4) are then applied to the physical vortices, taking into account the velocities induced by the virtual vortices, and are advanced in time with an explicit Euler scheme. This procedure is implemented in MATLAB with a nondimensional time step $\Delta t = 0.1$, $M = 201$ physical vortices, and $6M$ virtual vortices. The simulation is initialized with a small vertical displacement of the center physical vortex and the total integration time is 20. The localized initial perturbation generates a growing wave packet whose amplitude is defined as

$$A(x,t) = \sqrt{x_m(t)^2 + y_m(t)^2}, \tag{22}$$

where $m = \mathrm{round}(x)$. The growth rate observed along spatiotemporal rays $x/t = v_g$ emerging from the initial location of the perturbation can be evaluated from the amplitude at two distinct time instants t_1 and t_2 via

$$\sigma(v_g) = \frac{1}{t_2 - t_1} \ln\left[\frac{A(v_g t_2, t_2)\sqrt{t_2}}{A(v_g t_1, t_1)\sqrt{t_1}}\right]. \tag{23}$$

A simulation with confinement ratio $q = 0.8$ is first performed and the growth rate of the resulting wave packet is shown in circles in Fig. 4(a). The excellent agreement obtained between the numerical growth rate and that from the analytical dispersion relation validates the accuracy of the numerical method. We now carry out simulations of the impulse response for a range of confinement ratios and retrieve the leading- and trailing-edge velocity magnitude $|v_g^\pm|$ in each case. The results are displayed in circles in Fig. 4(b) and again compare extremely well with the velocities obtained previously from the analytical dispersion relation. The range for q is no longer limited at 0.9 and we can compute how the curve of $v_g^\pm$ quickly approaches the theoretical value of π that is readily obtained from the dispersion relation (11) for the unconfined single row of point vortices. This value was originally derived as an academic exercise by Huerre [44] and was previously reported in Ref. [32].

IV. SIGNIFICANCE FOR FREE SHEAR LAYERS

As mentioned in the introduction, a row of vortices results from the saturation of the primary instability of a free shear layer [1]. In this context, the SPI of the point vortex model studied in the previous section can be regarded as a model of the 2VPI of the mixing layer. However, since primary and secondary instabilities do not necessarily have the same absolute/convective character, they may be affected differently by confinement; this will have implications for the development of the shear layer. In the present section, we address what are these possible implications. We begin by comparing the spatiotemporal properties of the primary instability and the SPI.

A. Comparison with the primary instability of a tanh profile

Healey [6] considered the inviscid instability of a confined plane mixing layer profile of the form

$$U(y) = 1 + R \tanh\frac{y}{2}, \tag{24}$$

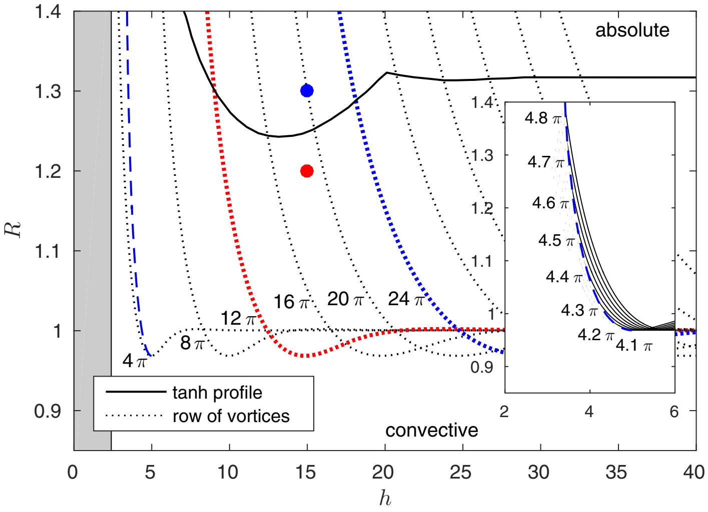

FIG. 5. Spatiotemporal behavior of the tanh profile (24) and the row of point vortices. Domains of absolute and convective primary instability (tanh profile) are separated by the critical velocity ratio R_{c1} (solid line), while in the gray region it is stable. Domains of absolute and convective instability of the SPI, separated by the critical velocity ratio $R_{c2,\lambda}$, are shown for different values of the intervortex spacing $\lambda = 4\pi, 8\pi, 12\pi, 16\pi, \dots, 44\pi$ (dotted lines). In both cases, values of R greater (lower) than the reported critical value lead to absolute (convective) instability. The $R_{c2,\lambda}$ determine the critical velocity ratio of the 2VPI to the right of $\bar{R}_{2C}$ (dashed line), below which the 2VPI is always convective. The inset shows a close-up around $\bar{R}_{2C}$ including various intersecting $R_{c2,\lambda}$ (solid lines). Results for the primary instability are from Healey [6].

where U is the base flow velocity in the x direction, y is the cross-stream direction, and $R = (U_1^* - U_2^*)/(U_1^* + U_2^*)$ is a velocity ratio with U_1^* and U_2^* the dimensional velocities far above and below the mixing layer. Velocities are nondimensionalized with the average advection velocity $\bar{U}^* = (U_1^* + U_2^*)/2$, and lengths are nondimensionalized with the shear layer thickness δ. Symmetric confinement by horizontal parallel plates is enforced by free slip boundary conditions at $y = \pm h$. Note that $2h\delta = d$. In this setting, Healey showed that confinement has a stabilizing effect on the temporal stability of the mixing layer but can increase the region of absolute instability in a certain range of h. The critical velocity ratio R_{c1} (c and 1 for "critical" and "primary") that separates regions of absolute and convective instability obtained by Healey for the tanh profile Eq. (24) is shown by the solid line in the (h, R) plane in Fig. 5. For the strong confinement shown in the shaded region of Fig. 5, the primary instability is no longer present.

Returning to our model of point vortices, the increase of $|v_g^{\pm}|$ with increasing confinement observed in Fig. 4(b) indicates a similar destabilizing effect of confinement on the secondary instability of the mixing layer. In order to compare quantitatively the convective/absolute behavior of this SPI with the primary instability results from Fig. 5, we need to relate dimensional quantities in our point vortex model with their mixing layer counterparts. If the single row of vortices emerges out of the saturating mixing layer, we can equate the circulation per unit length of both systems to get

$$\frac{\Gamma}{a} = -(U_1^* - U_2^*). \tag{25}$$

Placing ourselves in the laboratory frame, in which the vortices are advected at the mean velocity of the mixing layer $\bar{U}^*$, the dimensional front velocities of an impulse response wave packet in the row of vortices is

$$v_f^{\pm *} = \bar{U}^* + v_g^{\pm *} = \bar{U}^* - \frac{\Gamma}{2\pi a} v_g^{\pm}, \tag{26}$$

where $v_{f,g}^- < v_{f,g}^+$, the $v_g^{\pm *}$ are the dimensional leading- and trailing-edge velocities of the impulse wave packet in the reference frame of the vortices, and $v_g^\pm$ are their nondimensional counterparts displayed in Fig. 4(b). We now nondimensionalize (26) with $\bar{U}^*$ and make use of (25) to obtain

$$v_f^\pm = 1 + \frac{U_1^* - U_2^*}{2\pi \bar{U}^*} v_g^\pm = 1 + \frac{R}{\pi} v_g^\pm. \tag{27}$$

The row of vortices becomes convectively unstable in the laboratory frame when v_f^- turns positive. This allows us to formulate a critical velocity ratio for the SPI, R_{c2}, above which the single row of point vortices undergoes convective to absolute transition

$$R_{c2} = \frac{\pi}{|v_g^-|}. \tag{28}$$

Finally, in order to compare R_{c1} with R_{c2}, we need to relate lengths from the point vortex model to those in the mixing layer. Having in mind that we aim at modeling the 2VPI, it appears at first reasonable to equate the dimensional intervortex spacing a with the wavelength of the temporally most unstable primary perturbation of the mixing layer. However, this would amount to prescribing a unique wavelength selection to the primary instability, whereas in real mixing layers the wavelength selection is a complex dynamical process involving various factors. For now, we leave a as an arbitrary parameter, considering first the SPI of a general row of vortices independently of how it was formed.

We relate the aspect ratio q of our model to the length scale of the mixing layer through the distance between the confining plates at $y = \pm h$ as

$$q = \frac{d}{a} = \frac{2\delta h}{a} = \frac{2h}{\lambda}, \tag{29}$$

where the intervortex spacing is now given by $\lambda = a/\delta$. For any given vortex separation distance λ, one can combine (28) and (29) with the data from Fig. 4(b), which determines a family of critical velocity ratios $R_{c2,\lambda}(h)$ that separate regions of absolute and convective vortex pairing instability in the (h, R) plane. Critical curves $R_{c2,\lambda}$ for different values of the intervortex spacing $\lambda = 4\pi, 8\pi, 12\pi, 16\pi, \ldots, 44\pi$ are plotted in dotted lines in Fig. 5. A remarkable aspect of these $R_{c2,\lambda}$ curves is the possibility of absolute instability with $R < 1$, that is, without counterflow. This promoted absolute instability takes place around $h \approx \lambda/2.5$.

According to the results plotted in Fig. 5, all possible combinations between absolute or convective instability for the tanh profile and the SPI are in principle possible for different values of λ, R, and h. For example, if $(h, R) = (15, 1.3)$ and $\lambda = 24\pi$, depicted in blue, the (primary) instability of the tanh profile is absolute while the (would-be secondary) SPI is convective. Since we are interested in the SPI as a model for the 2VPI, we refer to this situation as 1A2C. If we then change the R and λ values to $R = 1.2$ and $\lambda = 12\pi$, depicted in red, we would have the opposite situation in which the tanh profile instability is convective and the SPI is absolute (1C2A). The remaining possibilities 1A2A (both instabilities absolute) and 1C2C (both convective) are present in the (h, R) plane.

Let us now consider the possible sequence of instabilities in a mixing layer; i.e., we now view the SPI as the 2VPI forming from the outcome of the primary instability of the shear layer. Given the appropriate initial conditions or forcing, it is in principle conceivable that a vortex row be formed with any intervortex spacing lying within the range of unstable wave numbers of the primary instability. Thus, the relevant range of λ can be taken as given by the range of temporally unstable wave numbers of the tanh profile. In the confined case, this unstable range is given by Healey [6] (see his Fig. 1) and goes from $k = 2\pi/\lambda = 0$ up to an h-dependent critical wave number $k_c(h)$ which decreases with h until it goes to zero at $h \approx 2.399$. This yields the stable shaded region in Fig. 5. In Fig. 5, the plotted $R_{c2,\lambda}$ curves correspond to wave-number values $k = 1/2, 1/4, 1/6, \ldots, 1/22$. Apart from $k = 1/2$, which is the critical wave number k_c in the unconfined case, these values are within the range of temporally unstable wave numbers when h is not too small. Thus, their corresponding $R_{c2,\lambda}$ curves are potentially valid critical curves for the 2VPI of a tanh shear layer, unlike the $\lambda = 4\pi$ curve since the wavelength issuing from the primary instability must be larger. The region of applicability to the 2VPI of the $R_{c2,\lambda}$ family of critical curves (of the SPI) is limited by the dashed line of Fig. 5, which translates to the present context the critical wavelength $k_c(h)$ of the tanh profile given by Healey [6]. We denote the corresponding function as $\bar{R}_{2C}(h)$ since for R below its curve the secondary instability is necessarily convective, as explained in detail in Appendix B.

B. Discussion

Above and to the right of $\bar{R}_{2C}$ it is, depending on λ, still possible to have all combinations between absolute and convective for the primary and secondary instabilities. Among these cases, the most commonly observed in coflowing mixing layer experiments is 1C2C, for which the primary and a number of 2VPIs succeed each other spatially in a facility-dependent way due to a high sensitivity to incoming noise [3]. In this case, vortex merging events will increase the wavelength λ thus selecting curves $R_{c2,\lambda}$ which move successively to the right in Fig. 5 and the instability generally remains convective.

The same situation for the secondary instability would occur in case 1A2C, except that the initial wavelength λ_0 of the vortex row would be robustly selected by the absolute primary instability. This selected wavelength λ_0 can be expected to correspond to the real part of the absolute wave number of the primary instability k_0, although nonlinear effects, strong forcing, or initial conditions could also have an effect. Thus, it would be possible to define a unique critical curve R_{c2,λ_0} that would be valid in the region 1A. However, this involves finding in the complex k plane the absolute wave number of the tanh profile as a function of R and h, which goes beyond the scope of the present paper. We leave instead λ as a free parameter and proceed to discuss the cases 1A2A and 1C2A wherein the 2VPI is absolute (2A).

The cases 2A fall in the relatively unexplored situation of an absolute secondary instability and the outcome is not obvious. One possibility of this absolute 2VPI would be the scenario of Chomaz [15,36], discussed in the introduction, of a sudden one-step transition to a complex behavior. Examples discussed in Ref. [36] include the emergence of low-frequency oscillations of the saturated nonlinear state of a complex Ginzburg-Landau model (on this model, see also Ref. [35]) and a mixing layer. These are somewhat reminiscent of low-frequency modulations observed in 2D wakes [47] or forced capillary jets [48], Sec. IV.B; the possible relation of these phenomena with absolute secondary instabilities is an open question that requires a dedicated study of each particular case. In the case of mixing layers, we can re-evaluate this scenario in the presence of confinement.

1. A tentative wavelength selection mechanism

Without resorting to a full study involving experiments or nonlinear simulations, it is possible to analyze in some more detail the possible outcome of an absolute 2VPI. One important consideration is that the nonlinear development of the instability leads to the merging of neighboring vortices. As mentioned at the beginning of this discussion, vortex-merging events will increase the wavelength λ while moving the relevant critical curve $R_{c2,\lambda}$ to the right in Fig. 5. This can be better represented in the $(R,\lambda/h)$ plane of Fig. 6, in which the family $R_{c2,\lambda}$ separating the regions of absolute and convective instability for the SPI collapses into a single critical curve. Increasing λ due to vortex merging translates then directly into moving upwards in the $(R,\lambda/h)$ plane. Figure 6 shows that every point in region 2A is located below region 2C. Thus, if an initial λ/h is such that the 2VPI is absolute (2A), increasing λ through successive vortex pairings will eventually bring the system into the convective region 2C, in which it will remain for the subsequent mergers that may occur. An example of this process is depicted in Fig. 6, in which the initial λ/h is doubled twice while undergoing two pairings before getting out of region 2A into 2C.

In a spatially developing shear layer, the process of finite successive pairings drawn in Fig. 6 is, however, more complex to interpret since it is intrinsically a transient phenomenon, leading eventually to a convectively unstable row of vortices. Thus, an absolutely unstable row of vortices could be observed but only at intermediate times. Indeed, the process of finite pairings could be

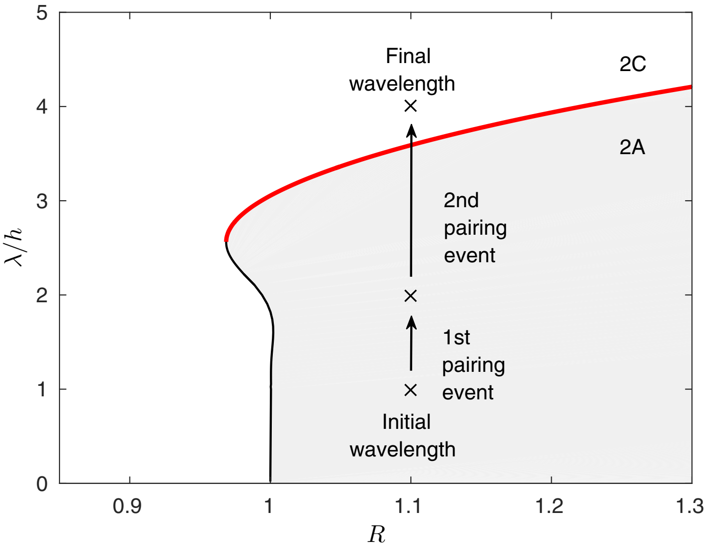

FIG. 6. Tentative scenario for wavelength selection. If the ratio λ/h of intervortex spacing to midchannel width is such that the secondary instability is absolute (2A), successive vortex pairings will increase λ and eventually bring the system in the region where the secondary instability is convective (2C), in which it will remain. According to this interpretation, a spatially developing mixing layer with counterflow ($R > 1$) can only exhibit a row of vortices if λ/h is large enough to fall in the region 2C.

observed as depicted in Fig. 6 if the "initial wavelength" lies within the 2A region, resulting, for example, from a sudden modification of the confinement. But the more relevant question concerns the nature of the permanent regime in which a spatial shear layer settles in the long time limit.

In the long time limit, and after a complex sequence of spatiotemporal pairing events, one expects that the 2VPI becomes convective. Indeed, this possible outcome is consistent with the fact that the saturation of the 2VPI leads to a similar row with double the wavelength, which falls also in the unstable range of the primary instability. Given the nature of its dispersion relation, any large wavelength λ could be a result of the primary instability, regardless of how far apart the vortices are. Thus, it should be possible for the primary instability to bypass the wavelengths that yield absolute 2VPI by spatially saturating directly on a wavelength which is large enough so that the 2VPI is convective. In other words, it could be possible, at least in principle, to construct a global mode with a spatial front connecting a parallel shear layer at the inlet with a row of vortices that are sufficiently far apart to lie in the 2C region.

According to this scenario, the practical consequence of the region of absolute secondary instability is to restrict the range of possible wavelengths present in the permanent state of a shear layer with counterflow. According to this wavelength selection mechanism, a spatially developing mixing layer reaching a permanent regime can only exhibit a row of vortices with wavelength λ if $\lambda/h = 2/q$ is large enough to fall in region 2C. This would imply that vortex rows in spatial mixing layers with counterflow ($R > 1$) can only occur below a sufficiently small confinement ratio, $q = 2h/\lambda$, given by twice the inverse of the critical line in Fig. 6, i.e., when the confinement is strong enough.

One consequence of this wavelength selection mechanism is the impossibility of having a spatial row of vortices with zero mean flow, i.e., in the limit $R = \infty$; one may expect that this eventually leads to the merger of all vortices into one large vortex. This ultimate merging process is related to the fact that in the point-vortex model used in this work, the instability persists for arbitrarily strong confinement. More realistic models are expected to relax this anomaly, as further explained in the next section. More interestingly, another consequence is the impossibility of creating spatial mixing layers with finite counterflow ($R > 1$) in the absence of confinement. Indeed, according to the critical curve of Fig. 6, for $1 < R < 1.3$ the distance between consecutive vortices should be more than about three to four times the distance from the center of the shear layer to the symmetrically confining walls.

2. Shortcomings and applications

We close this discussion with some comments on the validity of this highly idealized, inviscid point-vortex model to real viscous shear flows. Indeed, the model contains the minimal features required to study the effects of confinement on the 2VPI and it is not expected to be quantitatively valid. There are various aspects that should modify our results, notably viscosity and real vortices' finite size. In the absence of confinement, these two effects are taken into account in the computations of the SPI on Stuart vortices of Ref. [32]. Their computations with $\mathrm{Re} = 500$ show that the critical velocity ratio R decreases monotonically from its value for parallel flow as the vortex concentration increases (see Fig. 4 in Ref. [32] or Fig. 12 in Ref. [36]). Following the same trend, one can expect the family of critical curves $R_{c2,\lambda}$ to move upwards in Fig. 5, but remaining below the primary instability curve in the unconfined limit. Accordingly, the single wavelength selection curve in Fig. 6 would move to the right; this will be of relevance for the discussion below. Aside from the temporal instability being present for arbitrarily strong confinement (as $q \to 0$, see Sec. II B) and the potential for absolute instability without counterflow (i.e., $R_{c2,\lambda} < 1$), every other qualitative aspect can be expected to remain unchanged from these two effects.

Another important effect that is not taken into account in the present model is the no-slip condition at the walls. These would generate boundary layers that can be seen as a source of vorticity that could affect the whole flow, as occurs for the inverted Kármán street behind a confined obstacle [49]. In view of the experimental possibility of generating plane shear layers with counterflow, the possibly disrupting effect of boundary layers at the confining walls can be minimized with moving walls. In this regard, moving walls are also likely to be important for driving the flow at different velocities without generating a transverse pressure gradient. In fact, the inability to capture the effects of such pressure gradients is another important shortcoming of our model. Nevertheless, point-vortex models are a good first approximation for 2D vortex dynamics at large scales; these large scales are the least affected by viscous effects, and they are indeed the ones involved in the 2VPI. Regarding the stability of viscous shear flows, the pertinence of point-vortex models is further supported by our previous results [31] on the spatiotemporal stability of the Kármán street, and by recent experiments [34] showing the stabilizing effect of confinement on vortex streets. These experiments have validated results from the 1920s [50] on the stability of streets of point vortices.

A transverse pressure gradient seems like a natural explanation of the failure in the attempt to obtain a spatial mixing layer with counterflow by Humphrey and Li [26]. Our wavelength selection mechanism provides an additional reason (or an alternative explanation) for why their experiment could not result in a permanent regime with a counterflowing mixing layer, even if it had been driven by moving walls instead of opposite pressure gradients. They [26] report observations with the same flow rate in both directions, i.e., with zero mean flow, and they also note that "unequal flow rate observations did not differ fundamentally from the results presented." (p. 467) The reported streamwise length of their free shear layer was 7.62 cm, only slightly larger than the distance of 5.08 cm to the confining walls. In fact, this is not enough to accommodate even a pair of vortices that would not be absolutely unstable. Because of the different geometry, our results do not apply to the experiments of Strykowski and collaborators [17,27]: The celebrated experiment of Ref. [17] was on cylindrical jets, and subsequent experiments on plane mixing layers with counterflow use asymmetric and nonparallel confining walls [27]. Interestingly, our results do suggest that it could be possible to experimentally generate plane shear layers with counterflow, but for this to be achieved the mixing layer needs to be sufficiently long in the streamwise direction with respect to the vertical distance between the confining walls.

A dedicated study of this prediction would have to involve nonlinear simulations and experiments, going beyond the scope of the present paper. However, in view of our proposed scenario, we can reassess the mixing layer results presented by Chomaz [36] in support of the different scenario of a one-step transition to complex behavior. In his Fig. 8, Chomaz shows successive images of a shear layer with $R = 1.42$ at Reynolds number 400 kept artificially parallel by a diffusion-canceling body force and confined with freely slipping walls. The initially parallel shear layer is seen to develop KH vortices, first at its downstream end and subsequently moving upstream. The details of the upstream displacement of the emerging row of vortices cannot be ascertained from the images shown, but vortex pairings are clearly present and the distance between consecutive vortices increases in time. About the resulting flow, Chomaz notes that "the Global Mode for the mixing layer does not seem to be stable" (p. 392) [36], and he describes it as displaying random pairings (in Refs. [15,36], see the last quotation of the introduction). Based on the results for the absolute/convective instability of Stuart vortices without confinement [32], Chomaz attributes this randomness to the alleged absolute nature of the pairing instability, analogous to what was observed in the Ginzburg-Landau model [35,36].

We can now provide a different interpretation of Chomaz's results. Indeed, it is likely that this transient process shown in Fig. 8 of Ref. [36] corresponds to the proposed process depicted in Fig. 6. Chomaz's numerical experiment with an initially parallel shear layer with counterflow seems, as in a sudden modification of the confinement, like the kind of conditions leading to an absolute "initial wavelength" in which one would expect to observe the occurrence of this transient process. The parallel shear layer is first subject to the primary instability which, by the snapshot at time 300 of Fig. 8 of Ref. [36], has developed into a row of vortices that is subsequently subject to pairing through an absolute 2VPI. Vortex separation increases after pairing, and one can calculate the confinement ratio from the final snapshot at time 500 of the figure. The separation λ between the closest pair of vortices is then about four times the midwidth h of the channel. Considering the velocity ratio $R = 1.42$ and the finite size of the vortices that, as discussed above, favors convective instability with respect to point vortices (Fig. 4 of Ref. [32] or Fig. 12 in Ref. [36]), this value is very likely close to the absolute/convective instability threshold of a more realistic row of vortices (with the curve in Fig. 6 displaced to the right). Thus, it is possible that the final state of the spatial shear layer observed by Chomaz [36] is only convectively unstable (case 1A2C) and that the observed randomness is a result of the high sensitivity to small disturbances characteristic of convectively unstable flows (as in the case of the "secondary vortex street" studied in Ref. [51]). This is, in our view, the most likely consequence of the absolute/convective nature of the 2VPI.

As shown, our results make it possible to provide a simple reassessment of the previous results of Refs. [26,36] based on simple geometry. For the experiments of Humphrey and Li [26], the aspect ratio of their test section cannot possibly lead to a saturated free-shear layer (in the usual form of a row of vortices) that is not absolutely unstable; the flow accordingly developed a complex spatial structure unlike that of mixing layers. The case for the simulations of Chomaz [36] is different; the long and narrow domain led to a permanent regime of consecutive vortices with a complex time dependence. While the very different conditions between these two cases do not allow us to draw conclusions, they serve to exemplify the main potential applicability of our results: providing a design criterion for achieving planar mixing layers with counterflow. As hinted above, and given that our criterion favors long domains, it appears essential that the different streams be driven by drag and not pressure, for otherwise the flow will likely result in a large stagnant region. The recent experiments testing the stabilization by confinement of stationary Kármán streets [34] could be adapted to test our prediction.

V. SUMMARY AND CONCLUSIONS

We have characterized the effect of confinement on the absolute/convective nature of the pairing instability based on the infinite row of point vortices. This is a minimal model to study how the growth of free shear layers through successive pairings can be eventually limited by the effects of confinement. Surprisingly, as shown in Sec. II B, the pairing instability is never fully stabilized by confinement in this conservative model, the temporal growth rate of the instability becoming instead exponentially small as confinement or, equivalently, vortex separation increases. This behavior is well captured with an approximate expression for the dispersion relation [Eq. (10)] that is asymptotically valid in this limit of strong confinement $q \to 0$.

This asymptotically valid dispersion relation also quantitatively captures the critical velocity, marking the threshold between absolute and convective instability for values of confinement up to $q \approx 0.69$. In order to compute the thresholds, the growth rate of the impulse response as observed in different reference frames is obtained from the (full and approximate) dispersion relations in a single frame. For this we develop an approach, described in Sec. III A, whereby the imaginary part of the wave number k_i and the relative velocity of a moving frame v are related as conjugate variables through a Legendre transformation of the growth rate ω_i evaluated on the locus of absolute wave numbers. The obtained results are confirmed with numerical simulations of the linearized impulse response. These simulations do also extend the computed results to the moderate and weak confinement regime ($q \gtrsim 1$), for which the evaluation of the dispersion relation in the complex plane fails due to divergence of the required series. We can thus compute the critical velocity for absolute/convective instability for all confinement values, including the approach to the previously known result for the unconfined limit [32,44].

Similar to the results on the tanh profile reported previously by Healey [6], we obtain a range in which the effect of confinement is to increase the propagation velocity of the instability, thus rendering it potentially absolute in conditions where it would be convective without confinement. This leads to the surprising possibility of absolute instability without counterflow. However, this particular aspect is likely related to the particular model of point vortices since, without confinement, the results of Brancher and Chomaz [32] for the model of Stuart vortices show that the propagation of the instability is slower with less concentrated vortices (see their Fig. 4). Still, the results of Ref. [32] are consistent with ours in that the secondary instability becomes absolutely unstable with less counterflow than the primary instability. This suggests that in a more realistic model the quantitative values will differ, but the overall picture can be expected to remain valid.

Assuming values of the midchannel width h that are not too small, the primary and secondary instabilities are, as expected, both absolute (1A2A) or both convective (1C2C) for sufficiently large or small values of the velocity ratio R, respectively. However, the region of absolute/convective instability for the pairing instability cannot be determined unequivocally in the (h, R) plane, because the threshold depends on the intervortex spacing λ. This intervortex spacing physically corresponds to the wavelength selected by the primary instability, or by previous instances of the secondary vortex pairing instability, and is therefore left in the analysis as a free parameter to be determined by the dynamics. As a result, situations 1A2C or 1C2A are both possible depending on the values of the velocity ratio R and wavelength λ (Fig. 5). Fixing R sets the absolute/convective nature of the primary instability, but the pairing instability can generally still be absolute or convective depending on the wavelength λ. For sufficiently small λ, the secondary pairing instability becomes absolute with less counterflow than the primary instability. Increasing the wavelength λ, as it would occur through vortex pairings, eventually leads to the pairing instability becoming only convectively unstable.

Cases in which the secondary pairing instability is convective have a predictable outcome: The row of vortices issuing from the saturation of the primary instability will be sensitive to incoming disturbances and exhibit irregular pairings as the vortices are advected downstream. In the common case of coflowing shear layers [3], the primary instability is also convective (1C2C) and the primary row of vortices typically also irregular. The situation will not change dramatically if the primary instability is absolute (1A2C), as in the case of the Bénard–von Kármán street in the cylinder wake [31]; the secondary pairing instability might then still develop irregularly while advected on a regular row of vortices.

Cases of absolute secondary instability are less straightforward and should be generally studied on a case-by-case basis. A generic scenario that has been proposed is that of a sudden transition to complex behavior [15,36]. This has been argued to be the case for free shear layers, for which the secondary instability is absolute before the primary instability in the absence of confinement [32]. However, for the present secondary instability, which is subharmonic, the increase in wavelength through successive pairings will also increase the effects of confinement, eventually leading to the instability becoming convective. In addition, since the primary instability is active for arbitrarily large wavelengths, its spatial saturation could bypass the smaller wavelengths that are absolutely unstable, leading directly to a row of vortices that is only convectively unstable. This constitutes a mechanism of wavelength selection, which we propose for spatially developing shear layers with counterflow.

According to this wavelength selection mechanism, the wavelength of the ensuing vortex row must be sufficiently large so that the secondary pairing instability is convective. As a consequence, spatially developing rows of vortices, which respect the global flow structure of mixing layers, are only possible with a confinement strong enough for the pairing instability to be convective; this amounts to the requirement of a sufficiently long and narrow domain. This prediction is consistent with the numerical results of Ref. [36] and with the failed experimental attempt of Ref. [26], providing a guideline for the experimental and numerical search for shear layers with counterflow. Indeed, together with the transverse pressure gradient that unavoidably results from putting in contact two opposite pressure-driven flows, this mechanism is likely related to the lack of experimental realizations of spatial shear layers with counterflow.

In conclusion, we propose a rationale for explaining what are the conditions under which it can be possible to obtain spatial shear layers with counterflow. Our results, however, being obtained in the highly idealized model of point vortices, are not expected to be quantitatively valid. Still, experimental observations of a confined Bénard–von Kármán vortex street [34] in the absence of advection have recently vindicated old predictions for the stability of these confined vortex streets based on von Kármán's point vortex model [50]. Also, our previous results reconciling Kármán's point vortex model with ubiquitous observations of vortex streets [31] further supports the utility of models of point vortices for studying hydrodynamic instabilites.

Obvious ways in which the present results could and should be extended involve asymmetric confinement and more realistic vortex street models, including but not limited to Stuart vortices with finite core size. The latter should lead to more accurate predictions for wavelength selection, and the details of the proposed mechanism could be then tested with numerical simulations. But ultimately, it should be the failure or success of experimental tests which shall eventually confirm or falsify our predictions. In this regard, soap films or an adaptation of the recent experiments [34] proving the stability of confined vortex streets seem promising.

ACKNOWLEDGMENT

C.A. acknowledges the support of the Swedish Research Council Grant No. 638-2013-9243.

APPENDIX A: LEGENDRE TRANSFORM METHOD APPLIED TO KÁRMÁN'S STREET OF POINT VORTICES

In this Appendix, we present the application of the method developed in Sec. III A to a system with a more complicated dispersion relation than that of the confined single row. Specifically, we consider the dispersion relation of the unconfined and inviscid Kármán street of point vortices [22,31,33] given by

$$\omega = \pm A + s\sqrt{B^2 - C^2}, \tag{A1}$$

where $+A$ and $-A$ correspond to symmetrical and antisymmetrical modes respectively, $s = \pm 1$ gives two solution branches for each mode, and the coefficients A, B, and C are expressed as

$$A = \frac{1}{2}k(2\pi - k) - \frac{\pi^2}{\cosh^2 p\pi}, \tag{A2}$$

$$B = \frac{\pi k \sinh p(\pi - k)}{\cosh p\pi} + \frac{\pi^2 \sinh pk}{\cosh^2 p\pi}, \tag{A3}$$

$$C = \frac{\pi^2 \cosh pk}{\cosh^2 p\pi} - \frac{\pi k \cosh p(\pi - k)}{\cosh p\pi}, \tag{A4}$$

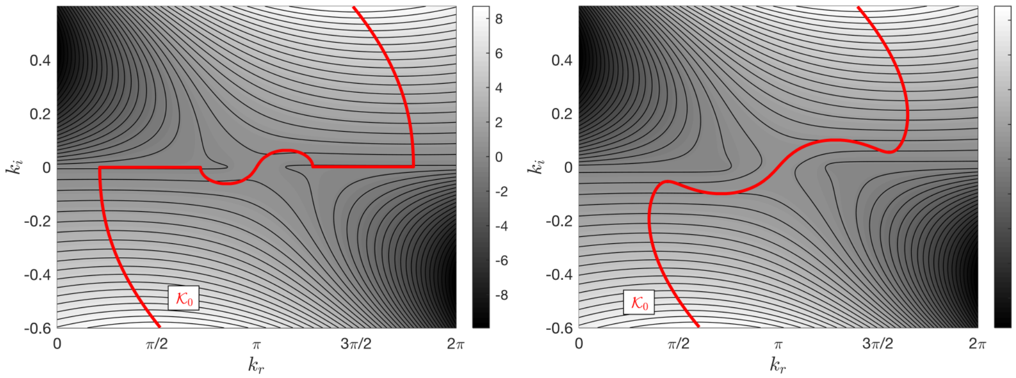

FIG. 7. Isocontours of ω_i in the complex k plane for the dispersion relation of the Kármán street (A1) with $p = 0.3$ (left) and $p = 0.316$ (right). The red line represents the locus $\mathcal{K}_0$ of absolute wave numbers defined by (19). Note that in both cases $\mathcal{K}_0$ contains multiple values of k_r for some intervals of k_i.

where p is the ratio of the vertical distance between the two rows of vortices to the horizontal distance between consecutive vortices in the same row. The wave number k of the perturbation is nondimensionalized by the inverse of the distance between consecutive vortices. In Fig. 7, we plot the contour levels of $\omega_i(k)$ from (A1) for $p = 0.3$ (left) and $p = 0.316$ (right), together with the locus $\mathcal{K}_0$ of absolute wave numbers defined by Eq. (19). Unlike the earlier case of the single row of vortices, here $\mathcal{K}_0$ contains multiple values of k_r for some intervals of k_i. We now apply the geometrical technique of Sec. III A for obtaining the growth rate of an impulse response wave packet along spatiotemporal rays $x/t = v$. First, we plot in Fig. 8 the curve $\omega_i(k^v_{0r}(k_i),k_i)$ for $p = 0.3$ (left) and $p = 0.316$ (right), which represents the imaginary part of the frequency along $\mathcal{K}_0$. Note that, as always in these plots, ω_i intersects the axis $k_i = 0$ at the maximum of the temporal growth rate. For the present dispersion relation, $\omega_i(k \in \mathcal{K}_0)$ is a multivalued function of k_i. At the point where $\mathcal{K}_0$ becomes parallel to the k_r axis and ω_i becomes multivalued, Eq. (20) prevents ω_i from becoming vertical, and it generically develops a cusp instead, as shown in Fig. 8 (right). Another possibility for this conservative system can be seen in Figure 7 (left), in which $\mathcal{K}_0$ coincides with the k_r axis for a finite distance and the tangent to $\omega_i(k^v_{0r}(k_i),k_i)$ has a discontinuity when touching the origin in Fig. 8 (left). Nevertheless, the monotonous behavior of $\partial\omega_i/\partial k_i = v$ along $\mathcal{K}_0$ ensures that every point on the locus corresponds to a unique value of v. This allows for the unambiguous determination of the growth rate of the impulse response wave packet based on (21) and the geometrical construction

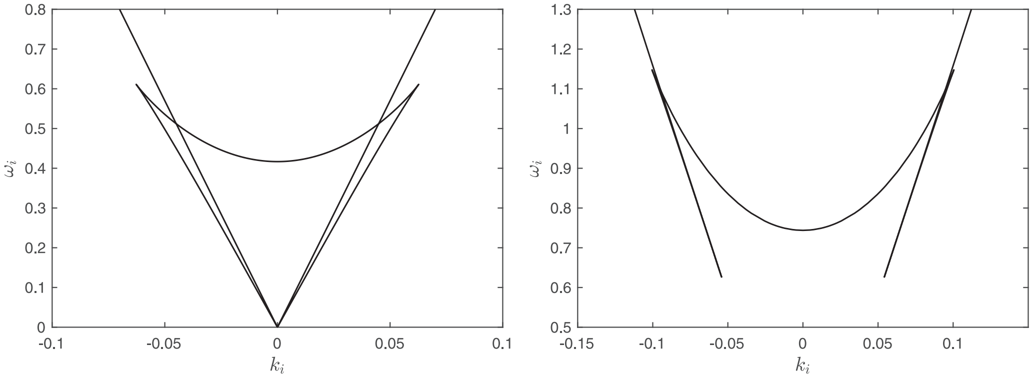

FIG. 8. Imaginary part of the frequency along the locus $\mathcal{K}_0$ of absolute wave numbers, expressed as a multivalued function $\omega_i(k^v_{0r}(k_i),k_i)$ of k_i for $p = 0.3$ (left) and $p = 0.316$ (right).

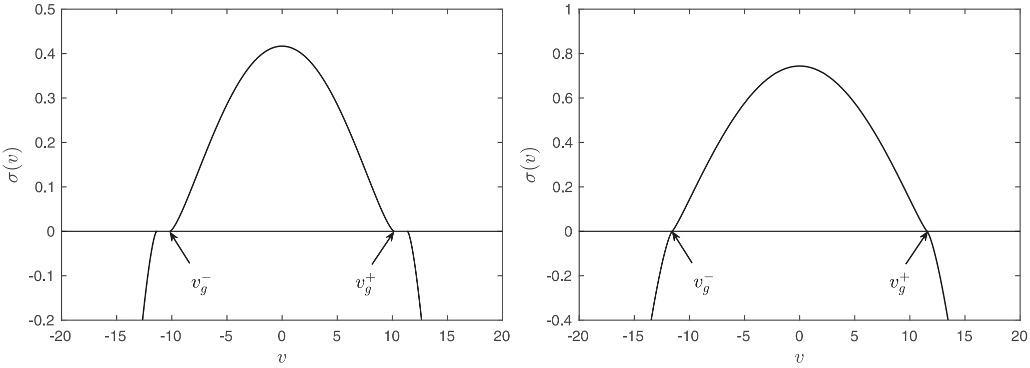

FIG. 9. Growth rate $\sigma(v)$ of the impulse response wave packet along spatiotemporal rays $x/t = v$ for $p = 0.3$ (left) and $p = 0.316$ (right). The streamwise extent of the wave packet is given by the leading- and trailing-edge velocities $v_g^{\pm}$ such that $v_g^{\pm} = 0$.

detailed in Sec. III A. The resulting curve $\sigma(v)$ is shown in Fig. 9 for $p = 0.3$ (left) and $p = 0.316$ (right).

APPENDIX B: DETERMINATION OF THE REGION WHERE THE SPI IS VALID AS A MODEL OF THE 2VPI

The SPI makes sense as a model of the 2VPI only when the vortex spacing λ is a wavelength unstable to the primary instability. The function $\bar{R}_{2C}(h)$, which delimits the region in which the $R_{c2,\lambda}(h)$ family describes different A/C regions for 2VPI, can be obtained as illustrated in the inset of Fig. 5. Take a value of $\lambda = \bar{\lambda}$ slightly larger than 4π (say, for example, $\bar{\lambda} = 4.4\pi$ shown in one of the continuous lines of the inset of Fig. 5, corresponding to $\bar{k} = 2\pi/\bar{\lambda} = 1/2.2$) and follow its corresponding $R_{c2,\bar{\lambda}}$ curve while decreasing h until the value $\bar{h}$ for which the corresponding $\bar{k}$ is critical for the tanh profile, i.e., the $\bar{h}$ such that $k_c(\bar{h}) = \bar{k}$. This determines $\bar{R}_{2C}(h)$ for $h = \bar{h}$ as $\bar{R}_{2C}(\bar{h}) = R_{c2,\bar{\lambda}}(h = \bar{h})$. Below this $\bar{h}$ the wavelength $\bar{\lambda}$ cannot result from the primary instability since it is stable for $\bar{k}$. Indeed, for an $h < \bar{h}$, the wavelength from the primary instability must be a $\lambda > \bar{\lambda}$, which would select a critical curve $R_{c2,\lambda}$ to the right of $R_{c2,\bar{\lambda}}$ that will not extend below $\bar{R}_{2C}(h)$. Conversely, if we fix h and take a value of R below the $\bar{R}_{2C}(h)$ curve, the primary instability will necessarily select a wavelength λ such that $R_{c2,\lambda}$ lies above $\bar{R}_{2C}(h)$, and the 2VPI will be convective.

[1] P. G. Drazin and W. H. Reid, *Hydrodynamic Stability* (Cambridge University Press, Cambridge, UK, 2004).
[2] G. L. Brown and A. Roshko, On density effects and large structure in turbulent mixing layers, J. Fluid Mech. **64**, 775 (1974).
[3] C. M. Ho and P. Huerre, Perturbed free shear layers, Annu. Rev. Fluid Mech. **16**, 365 (1984).
[4] A. Michalke, On the inviscid instability of the hyperbolic tangent velocity profile, J. Fluid Mech. **19**, 543 (1964).
[5] P. Huerre and P. A. Monkewitz, Absolute and convective instabilities in free shear layers, J. Fluid Mech. **159**, 151 (1985).
[6] J. J. Healey, Destabilizing effects of confinement on homogeneous mixing layers, J. Fluid Mech. **623**, 241 (2009).
[7] F. Gallaire, The effect of rounding corners or cutting edges on the absolute/convective instability properties of mixing layers, Eur. J. Mech. B Fluids **49**, 387 (2015).

[8] C. D. Winant and F. K. Browand, Vortex pairing: The mechanism of turbulent mixing-layer growth at moderate Reynolds number, J. Fluid Mech. **63**, 237 (1974).

[9] R. T. Pierrehumbert and S. E. Widnall, The two- and three-dimensional instabilities of a spatially periodic shear layer, J. Fluid Mech. **114**, 59 (1982).

[10] W. R. Peltier and C. P. Caulfield, Mixing efficiency in stratified shear flows, Annu. Rev. Fluid Mech. **35**, 135 (2003).

[11] C. Arratia, C. P. Caulfield, and J.-M. Chomaz, Transient perturbation growth in time-dependent mixing layers, J. Fluid Mech. **717**, 90 (2013).

[12] P. Huerre and P. A. Monkewitz, Local and global instabilities in spatially developing flows, Annu. Rev. Fluid Mech. **22**, 473 (1990).

[13] R. J. Briggs, *Electron-Stream Interaction with Plasmas* (MIT Press, Cambridge, MA, 1964).

[14] P. Huerre and M. Rossi, Hydrodynamic instabilities in open flows, in *Hydrodynamics and Nonlinear Instabilities*, edited by C. Godrèche and P. Manneville (Cambridge University Press, Cambridge, UK, 1998), pp. 81–294.

[15] J.-M. Chomaz, Global instabilities in spatially developing flows: Non-normality and nonlinearity, Annu. Rev. Fluid Mech. **37**, 357 (2005).

[16] R. J. Deissler, Noise-sustained structure, intermittency, and the Ginzburg-Landau equation, J. Stat. Phys. **40**, 371 (1985).

[17] P. J. Strykowski and D. L. Niccum, The stability of countercurrent mixing layers in circular jets, J. Fluid Mech. **227**, 309 (2006).

[18] M. P. Juniper, The effect of confinement on the stability of two-dimensional shear flows, J. Fluid Mech. **565**, 171 (2006).

[19] M. P. Juniper, The full impulse response of two-dimensional jet/wake flows and implications for confinement, J. Fluid Mech. **590**, 163 (2007).

[20] J. T. Stuart, On finite amplitude oscillations in laminar mixing layers, J. Fluid Mech. **29**, 417 (1967).

[21] A. K. M. F. Hussain, Coherent structures and turbulence, J. Fluid Mech. **173**, 303 (1986).

[22] P. G. Saffman, *Vortex Dynamics* (Cambridge University Press, Cambridge, UK, 1992).

[23] G. M. Corcos and F. S. Sherman, The mixing layer: Deterministic models of a turbulent flow, part 1: Introduction and the two-dimensional flow, J. Fluid Mech. **139**, 29 (1984).

[24] S. A. Thorpe, Experiments on instability and turbulence in a stratified shear flow, J. Fluid Mech. **61**, 731 (1973).

[25] V. Kibens, Discrete noise spectrum generated by acoustically excited jet, AIAA J. **18**, 434 (1980).

[26] J. A. C. Humphrey and S Li, Tilting, stretching, pairing, and collapse of vortex structures in confined counter-current flow, J. Fluids Eng. **103**, 466 (1981).

[27] D. J. Forliti, B. A. Tang, and P. J. Strykowski, An experimental investigation of planar countercurrent turbulent shear layers, J. Fluid Mech. **530**, 241 (2005).

[28] P. Huerre, On the absolute/convective nature of primary and secondary instabilities, in *Propagation in Systems Far from Equilibrium: Proceedings of the Workshop, Les Houches, France, March 10–18, 1987*, edited by J. E. Wesfreid, H. R. Brand, P. Manneville, G. Albinet, and N. Boccara (Springer, Berlin, 1988), pp. 340–353.

[29] J.-M. Chomaz, A. Couairon, and S. Julien, Absolute and convective nature of the Eckhaus and zigzag instability with throughflow, Phys. Fluids **11**, 3369 (1999).

[30] H. Bolnot, S. Le Dizès, and T. Leweke, Spatio-temporal development of the pairing instability in an infinite array of vortex rings, Fluid Dyn. Res. **46**, 061405 (2014).

[31] S. Mowlavi, C. Arratia, and F. Gallaire, Spatio-temporal stability of the Kármán vortex street and the effect of confinement, J. Fluid Mech. **795**, 187 (2016).

[32] P. Brancher and J.-M. Chomaz, Absolute and Convective Secondary Instabilities in Spatially Periodic Shear Flows, Phys. Rev. Lett. **78**, 658 (1997).

[33] H. Lamb, *Hydrodynamics*, 6th ed. (Cambridge University Press, Cambridge, UK, 1932).

[34] P. Boniface, L. Lebon, L. Limat, and M. Receveur, Absolute stability of a Bénard–von Kármán vortex street in a confined geometry, Europhys. Lett. **117**, 34001 (2017).

[35] A. Couairon and J.-M. Chomaz, Primary and secondary nonlinear global instability, Phys. D (Amsterdam, Neth.) **132**, 428 (1999).

[36] J.-M. Chomaz, Transition to turbulence in open flows: What linear and fully nonlinear local and global theories tell us, Eur. J. Mech. B Fluids **23**, 385 (2004).

[37] R. J. Lingwood, Absolute instability of the boundary layer on a rotating disk, J. Fluid Mech. **299**, 17 (1995).

[38] R. J. Lingwood, An experimental study of absolute instability of the rotating-disk boundary-layer flow, J. Fluid Mech. **314**, 373 (1996).

[39] B. Pier, Finite-amplitude crossflow vortices, secondary instability, and transition in the rotating-disk boundary layer, J. Fluid Mech. **487**, 315 (2003).

[40] B. Viaud, E. Serre, and J.-M. Chomaz, Transition to turbulence through steep global-modes cascade in an open rotating cavity, J. Fluid Mech. **688**, 493 (2011).

[41] S. Imayama, P. H. Alfredsson, and R. J. Lingwood, On the laminar-turbulent transition of the rotating-disk flow: The role of absolute instability, J. Fluid Mech. **745**, 132 (2014).

[42] E. Appelquist, P. Schlatter, P. H. Alfredsson, and R. J. Lingwood, On the global nonlinear instability of the rotating-disk flow over a finite domain, J. Fluid Mech. **803**, 332 (2016).

[43] I. Delbende, J.-M. Chomaz, and P. Huerre, Absolute/convective instabilities in the Batchelor vortex: A numerical study of the linear impulse response, J. Fluid Mech. **355**, 229 (1998).

[44] P. Huerre, DEA exam, Ecole Polytechnique (1992).

[45] G. Dee and J. S. Langer, Propagating Pattern Selection, Phys. Rev. Lett. **50**, 383 (1983).

[46] W. van Saarloos, Dynamical Velocity Selection: Marginal Stability, Phys. Rev. Lett. **58**, 2571 (1987).

[47] L. Biancofiore, F. Gallaire, and R. Pasquetti, Influence of confinement on a two-dimensional wake, J. Fluid Mech. **688**, 297 (2011).

[48] C. Horvath, C. Arratia, and M. L. Cordero, Measurement of the dispersion relation of a convectively unstable capillary jet under confinement, Phys. Fluids **27**, 114103 (2015).

[49] S. Camarri and F. Giannetti, On the inversion of the von Kármán street in the wake of a confined square cylinder, J. Fluid Mech. **574**, 169 (2007).

[50] L. Rosenhead, The Karman street of vortices in a channel of finite breadth, Philos. Trans. Royal Soc. London, Ser. A **228**, 275 (1929).

[51] B. Kumar and S. Mittal, On the origin of the secondary vortex street, J. Fluid Mech. **711**, 641 (2012).